PHYSICAL REVIEW C VOLUME 38, NUMBER 3 SEPTEMBER 1988

Elastic deuteron scattering and optical model parameters at energies up to 100 MeV

J. Bojowald, H. Machner, H. Nann, W. Oelert, M. Rogge, and P. Turek
Institut für Kernphysik, Kernforschungsanlage Jülich, D-5170 Jülich, Federal Republic of Germany

(Received 23 October 1987; revised manuscript received 25 April 1988)

Differential cross sections of elastic scattering of deuterons on the target nuclei ^{27}Al, ^{89}Y, ^{120}Sn, and ^{208}Pb were measured at $E_d = 58.7$ MeV and $E_d = 85$ MeV. "Best-fit" parameters in terms of the phenomenological optical model were extracted from the data including in addition differential cross section and analyzing power data from the literature. A set of global optical potential parameters is derived.

I. INTRODUCTION

In the interaction of a light ion with nuclei, elastic scattering is the largest of all partial cross sections. For projectile energies sufficiently above the Coulomb barrier, the elastic angular distribution is dominated by a diffractionlike pattern. It was realized[1] that this phenomenon is due to the finite size of the nucleus and the fact that nuclei are "partially transparent." In a simplified description of the process, the optical model replaces the many-body problem by a complex effective potential in a one-body Schrödinger equation. The success of the optical model to account for elastic nucleon scattering leads one to apply this model also to composite particle scattering. It is of special interest to probe the validity of the optical model for the elastic scattering of deuterons which are weakly bound composite particles.

Previous work either dealt with studies on best-fit parameters for single nuclei or with systematic investigations to derive energy and mass number dependences for the optical-model parameters. Such studies include data with unpolarized deuterons[2–6] as well as data including polarization.[7–13] Reference 14 gives a compilation of previous work. In most cases the analysis resulted in a satisfactory description of the differential cross sections. Further improvement in the description of the data was achieved by taking into account an imaginary spin-orbit term in the potential.[15] However, at a deuteron energy of 80 MeV the phenomenological analysis fails to reproduce both differential cross sections and analyzing powers simultaneously.[16] Because of the large number of potential parameters in the case of the deuteron optical potential, fits to the data can be produced with similar quality for quite different and partly unphysical potential parameters. This is especially true when no or only a few analyzing power data are included in the analysis. Furthermore, discrete and continuous ambiguities occur at low energies. Many analyses were performed with an *a priori* choice of certain parameters. Therefore, a comparison of results obtained in different works is rather difficult.

For these reasons, attempts have been made to derive theoretically a deuteron optical potential.[17–19] This is more complicated than in the case of nucleon- or α-particle scattering where satisfactory results have been obtained. Because of the low binding energy of the deuteron, one is dealing in elastic deuteron scattering effectively with a three-body problem, the target nucleus interacting with both nucleons of the deuteron. In particular, the breakup and different inelastic processes have to be taken into account. The Pauli principle is effective even at the present high energies as has been shown by Ioannides and Johnson.[20]

Early attempts in the framework of the folding model[17] neglected spin-orbit effects and the breakup of the deuteron; in comparison to phenomenological analyses they yielded potential depths which were 10–20 % deeper for the real part and rather shallow for the imaginary part. Keaton and Armstrong[18] took into account spin-orbit coupling of the nucleons and the *D*-state breakup of the deuteron. Important results of their work were (i) a tensor term in the deuteron optical potential, which is very sensitive to the breakup channel, and (ii) that the terms in the deuteron optical potential could have Saxon-Woods form or derivatives of it, respectively. More recent folding-model calculations[19] including various breakup channels and realistic nucleon-nucleon forces are able to give a reasonable description of different cross sections of elastic scattering, vector and tensor analyzing powers for 80 MeV deuterons scattered on ^{58}Ni (Ref. 21). However, serious discrepancies in the reproduction of data exist; thus the folding model is not without criticism as is discussed recently by Austern *et al.*[22] Further, the potentials of Refs. 19 and 21 cannot be expressed analytically and are, therefore, not appropriate for global analyses.

The analysis of the present data will be performed using a phenomenological optical potential with a Saxon-Woods form factor or its derivative in the potential terms. But the potential parameters or the starting values for the fit procedure, respectively, will be properly chosen in order to approximate the folding model according to Ref. 18.

This work presents data for elastic angular distributions on some target nuclei throughout the periodic table. The deuteron energy was chosen as high as 58.7 and 85 MeV, and the measurements were carried out up to backward angles even larger than the rainbow angle[23,24] in order to minimize discrete ambiguities as discussed in Ref. 24.

Starting from the present data we will derive a set of global potential parameters including cross-section data and analyzing power measurements from the literature.[5,11,16,21] We will compare the results with those of potential L of Ref. 13, to date the only one study for global potentials for elastic deuteron scattering in the present energy range.

II. EXPERIMENTS

A. The beam

The experiments were carried out with 58.7 and 85.0 MeV deuteron beams of the isochronous cyclotron JULIC. The beams were focused to the center of a scattering chamber with a beam spot of 1.5 mm diam. At a distance of 3 m downstream the beam was dumped into a well-shielded Faraday cup for current integration.

At small angles data were taken with a momentum-analyzed beam resulting in a beam energy resolution of $\Delta E/E=(2-4)\times 10^{-4}$, and typical beam currents of 10–50 nA. Large angle measurements were performed with the nonanalyzed beam ($\Delta E/E=3\times 10^{-3}$) and beam currents of 100–150 nA. Higher currents were not used to keep the background (due to neutrons and γ rays) low and the dead time of the data-taking system always below 3%.

The beam quality was checked from time to time by inserting a polyethylene target; a typical spectrum is shown in Fig. 1. Because of the kinematics of the scattering on hydrogen, the corresponding peak shape is very sensitive to energy resolution and angle divergence of the beam. The slit settings in the beam-transport system were optimized to achieve a narrow and symmetric peak shape for scattering on hydrogen with the analyzed beam. At the same time an energy resolution of $\Delta E/E=115$ keV or 0.14% was obtained for heavy nuclei and worse for lighter nuclei due to kinematic broadening (Fig. 2). From the peak shape of the elastic scattering on hydrogen we extracted an angle divergence of the beam of 0.28°.

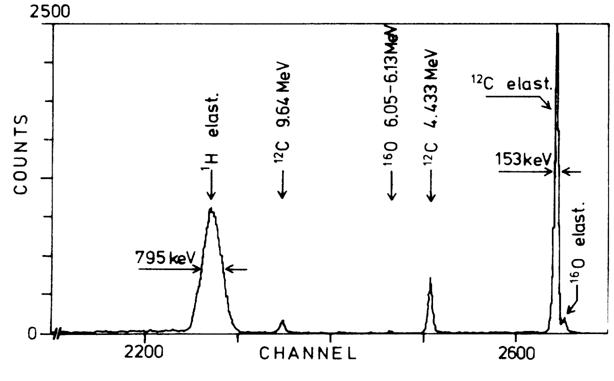

FIG. 1. Energy spectrum of 85 MeV scattered deuterons from a polyethylene target at $\theta=15°$. Peaks due to scattering on H, ^{12}C and ^{16}O contamination are indicated.

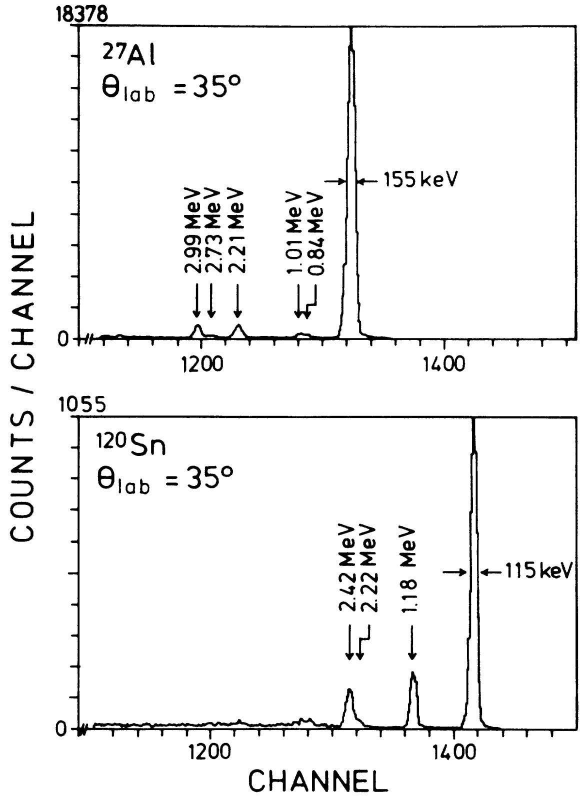

FIG. 2. Same as Fig. 1 but for the indicated targets and $\theta=35°$.

B. Experimental set up

1. Scattering chamber

The particle detectors were mounted outside the 20-cm-diam scattering chamber on a rotatable ring which pivots around the targets with a precision of 0.1°. Thus on their way to the detectors the scattered particles passed through (i) a 19-μm Mylar window, (ii) 1–7 cm of air depending on the detector position on the ring, and (iii) finally a 2.2-μm Havar window of the detector cryostat. The energy loss of 100–300 keV and energy straggling of 60–82 keV for the deuterons do not influence the elastic cross section. Because of the rapidly changing elastic angular distribution pattern, the scattering angle and hence the beam direction must be known to better than 0.2°. We observed deviations of the "0° beam direction" of up to ±0.4°. The slit system helped to reduce short-time variations of the beam. However, long-time variations of up to 0.2° within three days were still observed. Therefore, we measured in regular time intervals the scattering on the polyethylene target at fixed angles and deduced the precise scattering angle by the kinematics. Thus including corrections for the energy losses as discussed above, the scattering angle and the actual beam direction could be determined to less than ±0.1°.

2. *Targets*

The targets were positioned in the center of the scattering chamber. The vertical target positions of the different targets employed were reproducible up to 0.5 mm and the target angle to 1°.

The targets chosen were self-supporting foils of ^{27}Al, ^{89}Y, ^{120}Sn, and ^{208}Pb. In these nuclei, the first excited state is at least at 1 MeV excitation energy. The target thicknesses and isotopic abundances are listed in Table I. The areal density was measured in three ways: by weighing, by measuring the energy loss of α particles from a ^{244}Cm source, and by comparison of scattering data on two targets which were independently produced. These procedures result in an error for the target thickness of $\lesssim 6\%$.

3. *Detectors*

The detectors employed were commercial Si-surface-barrier detectors of 1000 μm thickness as ΔE detectors and home-made 20-mm-thick Ge(Li) detectors of the side entry type as E detectors.[25] Peak intensity losses from scattering out of the detector volume are expected to be negligible due to a favorable detector geometry chosen. In the initial state of each experiment the intensity of a low-energy tail due to nuclear reactions in the detector material and slit edge scattering on the apertures was determined. The peak intensity losses from reactions were taken into account[26] for the determination of the cross sections. Because of radiation damage the tail intensity increased during the runs. This was then compensated by applying a larger bias voltage. After typically four days of running, the detectors had to be regenerated.

The effective solid angle covered by the detector telescope was determined by a tantalum aperture with an inner diameter of 2 mm in front of the ΔE detector and was, depending on the distances chosen, between 0.41×10^{-4} sr at forward and 0.66×10^{-4} sr at backward angles. The corresponding openings in θ were 0.21° and 0.26°, respectively. To avoid background or slit scattering from the beam-transport system a second aperture with an opening of 4 mm diam was used, situated approximately 100 mm in front of the solid angle determining aperture.

Deuterons were selected by an electronic particle identification system. To detect the high-energy particles with reasonable counting rates the gain of the commercial preamplifiers was modified. Details were given elsewhere.[27]

Table I. Properties of the targets used.

Nucleus	Isotopic abundance (%)	Thickness (mg/cm^2) Weighing	α source
^{27}Al	100	2.6	2.69
		11.3	
^{89}Y	100	6.4	6.85
		8.03	
^{120}Sn	98.4	4.84	
		6.07	5.56
^{208}Pb	99.1	5.04	
		6.39	6.04

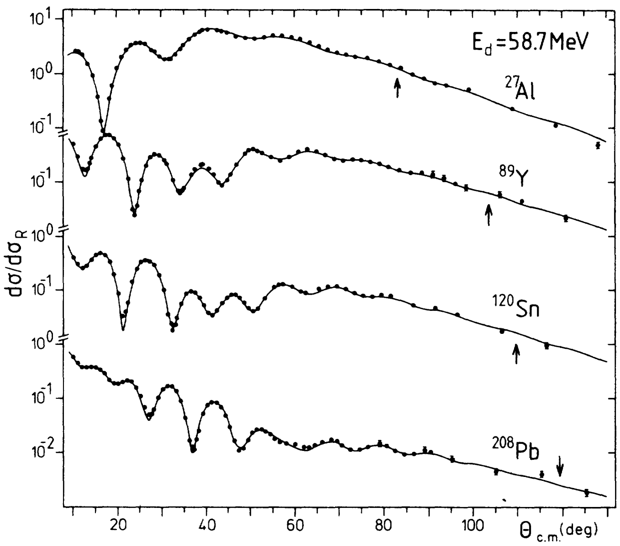

FIG. 3. Elastic angular distributions for the scattering of 58.7-MeV deuterons in terms of Rutherford scattering on nuclei indicated in the figure. The solid curve is an optical-model fit with parameters in Table II. The arrows indicate the positions of the rainbow angle.

4. *Experimental uncertainty*

Beam current and target thickness were monitored continuously by one counter at a fixed position. The following uncertainties contribute to the relative error between different values within one angular distribution: counting rate and dead-time correction result in a 3–4 %

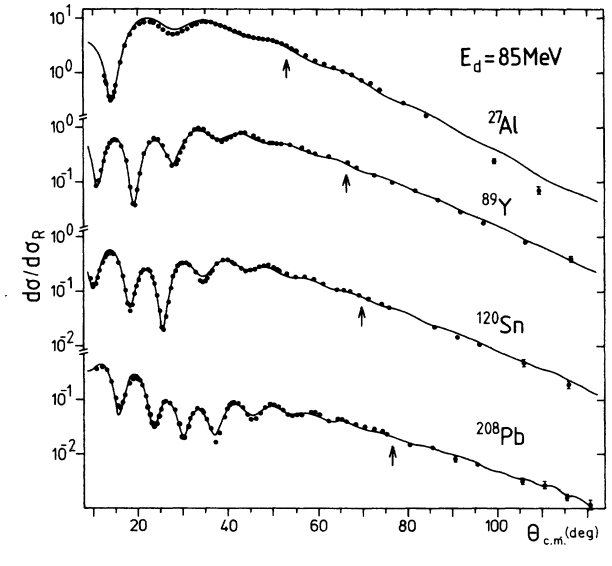

FIG. 4. Same as Fig. 3, but for $E_d = 85$ MeV.

total relative error which may increase to 5–6 % in the steep dropoff of the cross section due to the finite angular resolution. For angles larger than 100° the errors increased up to 20% due to poor statistics. The absolute values of the deduced cross sections include in addition the following uncertainties: beam current integration ($\leq 1\%$), solid angle ($\leq 2\%$), target thickness ($\leq 6\%$), and corrections due to losses in the detectors ($\leq 2\%$) leading to an overall absolute error of $\sim 7\%$ except for angles larger than 100°.

C. Experimental results

Two typical deuteron spectra both taken at the bombarding energy of 85 MeV are shown in Fig. 2. In the case of ^{27}Al, peaks are broader than for the heavier target nuclei due to kinematics. For all target nuclei investigated there is good separation between the ground and the first excited state.

The angular distributions for the elastic scattering measured for the four target nuclei are displayed in Fig. 3 for the lower bombarding energy of 58.7 MeV and in Fig. 4 for the higher bombarding energy of 85.0 MeV. The solid curves shown are the results of optical-model calculations which will be discussed below. The angular distributions show a diffraction pattern at forward angles which is washed out at the larger angles. Such a behavior is expected from the interplay between diffraction and refraction (rainbow scattering) of the incoming waves as can be explained, for instance, in semiclassical treatments.[23,24] In calculating the rainbow angles indicated by arrows in the figures spin-orbit effects were neglected for the sake of simplicity.

III. OPTICAL-MODEL ANALYSIS

The analytical expression of the potential form was

$$U(r)=V_c(r)-Vf_v(r,R_v,a_v)-i\left[W_{\mathrm{vol}}f_w(r,R_w,a_w)-4a_w W_{\mathrm{surf}}\frac{d}{dr}f_w(r,R_w,a_w)\right]$$
$$+V_{LS}\left[\frac{\hbar}{m_\pi c}\right]^2(\mathbf{l}\cdot\mathbf{s})\frac{1}{r}\frac{d}{dr}f_{LS}(r,R_{LS},a_{LS}) \qquad (1)$$

with the Saxon-Woods form factors

$$f_x=\{1+\exp[(r-R_x)/a_x]\}^{-1} \qquad (2)$$

and the nuclear radius

$$R_x=r_x A^{1/3}\ , \qquad (3)$$

where a_x denotes the diffuseness. The Coulomb potential V_c is taken as that of a charged sphere of radius $R_c=r_c A^{1/3}$. In the imaginary part of the potential, volume and surface absorption are used. The last potential term denotes the spin-orbit potential with a Thomas form. An imaginary spin-orbit potential[15,28] was not employed because we found that such a potential is rather weak. In addition to the vector term, three tensor terms may be introduced in the potential,[29] however, they were neglected in the present investigation since they have no influence on differential cross sections and vector polarization, the observables we are analyzing.

A. The method

Fits to the present data and to data from the literature[5,11,16,21] were performed by varying the optical-model parameters so as to minimize the quantity χ^2 separately for elastic cross section and analyzing power. In some cases the fits were searched simultaneously for both quantities, but minimizing χ^2 alone is not always a reliable criterion. A visual inspection of the agreement between all data and the fit calculation seemed to be preferred. Some *a priori* guidance for the parameters in the searches were employed to obtain physically meaningful solutions. Therefore, the parameter space was scanned by calculations on a grid to come close to the minimum χ^2 value. These values were used then as starting values for additional iterative searches. In all calculations the optical-model code MAGALI (Ref. 30) was employed. For the present energies, partial waves up to $l=40$ were included.

As has been pointed out,[32] there are two possibilities for determining optical-model parameters: best-fit parameters for a particular nucleus or global parameters valid for a large number of nuclei. We present both procedures. In choosing starting values for the parameters we will stick to the folding-model geometry as close as possible.

Following the folding model we chose as starting values for the real potential the sum of the nucleon potentials at half the bombarding energy. If elastic scattering cross sections were analyzed and only the real potential was adjusted the best fits resulted in one rather shallow χ^2 minimum. The best known continuous ambiguity is the correlation between the real potential depth and the radius parameters R_v, VR_v^x with $x\sim 2$. We have chosen starting values again from folding-model analysis, namely, $r_v=1.17$ fm and $r_w=1.30$ fm. It was found that the depth and the geometry of the spin-orbit potential cannot be determined unambiguously because it can draw strength from the real as well as the imaginary part of the potential. Such an effect was also found in the ^{3}He optical potential.[31] Even if analyzing power data are included in the analysis it is not possible to remove this ambiguity. It is, therefore, necessary to keep the spin-orbit parameters within reasonable limits.

Table II. Best-fit parameters with fixed geometry and pure surface absorption.

E_d (MeV)	Target	V (MeV)	a_v (fm)	W_{surf} (MeV)	r_w (fm)	a_w (fm)	V_{LS} (MeV)	r_{LS} (fm)	χ^2/N
85	^{208}Pb	80.9	0.84	13.9	1.18	0.98	7.9	1.05	1.29
	^{120}Sn	75.7	0.83	14.0	1.18	0.93	8.9	1.05	0.92
	^{89}Y	74.6	0.82	12.9	1.22	0.87	10.3	1.05	1.11
	^{27}Al	61.7	0.72	9.6	1.23	0.85	9.7	1.05	1.43
58.7	^{208}Pb	86.3	0.83	13.6	1.22	0.96	5.7	1.00	0.59
	^{120}Sn	82.9	0.83	13.4	1.22	0.91	6.2	1.00	0.92
	^{89}Y	81.6	0.81	12.5	1.25	0.84	7.3	1.00	0.72
	^{27}Al	70.9	0.72	10.0	1.27	0.83	8.4	1.00	0.48

$r_c = 1.30$ fm; $r_v = 1.18$ fm; $a_{LS} = 1.0$ fm.

B. Best-fit parameters

The values of the radius parameter r_v are scattered between 1.16 and 1.21 fm. In the best-fit analysis this parameter was chosen to be fixed to $r_v = 1.18$ fm. For the spin-orbit term we have chosen $r_{LS} \sim a_{LS} \sim 1.0$ fm and allowed only for small variations of r_{LS}. If we used starting values like $r_{LS} \sim 0.75$ fm and $a_{LS} \sim 0.5 r_{LS}$, a typical geometry in analyses at smaller deuteron energies,[9] we were unable to reproduce the data of the heavier target nuclei even if a mass dependence was included. Further, we assumed surface absorption only in the imaginary potential for the first time.

The extracted optical-model parameters are given in Table II. The corresponding fit curves are shown in Figs. 3 and 4. We observe (i) a decrease of r_w with energy and (ii) a mass dependence of the depth of the spin-orbit potential in contrast to the folding model.[18] This may be an indication that surface absorption only is inadequate. We therefore repeated the analysis with the geometry but with both volume and surface terms in the imaginary part. This procedure results in excellent fits. In this analysis we obtained values for V_{LS} of around 6 MeV in good agreement with the folding model. The average value of V_{LS} was slightly higher for $E_d = 58.7$ MeV than for $E_d = 85.0$ MeV; in agreement with folding model[18] we keep a fixed value of $V_{LS} = 6$ MeV. We reduced the number of free parameters further by fixing W_{vol} to the mean values $W_{\text{vol}} = 2.0$ MeV for $E_d = 58.7$ MeV and $W_{\text{vol}} = 5.0$ MeV for $E_d = 85$ MeV. For the radius parameter a statistical scatter of values between $r_w = 1.25$ fm and $r_w = 1.30$ fm showed up. We have chosen $r_w = 1.27$ fm as in folding-model predictions.[18] The extracted optical-model parameters of these fits are shown in Table III. The reproduction of the data is similar to the one shown above, but most χ^2/N values are better now.

C. Global potential

Starting with the constraints derived from the analysis of our data in the previous section we included data from the literature[5,11,16,21] into our considerations. We performed the analysis again in order to extract a global parameter set based on as much experimental data as possible. First, differential elastic cross-section data were analyzed, and in a second step, analyzing power data were included for a better determination of the spin-orbit potential term. Only data with elastic angular distributions

TABLE III. Best-fit parameters with fixed geometry and average values for the depths of volume absorption and the spin-orbit potential. Also included are the volume integrals and RMS radii of the real and imaginary potential.

E_d (MeV)	Target	V (MeV)	a_v (fm)	W_{surf} (MeV)	a_w (fm)	χ^2/N	$J_v/2A$ (MeV fm^3)	$<R_v^2>^{1/2}$ (fm)	$J_w/2A$ (MeV fm^3)	$<R_w^2>^{1/2}$ (fm)
85	^{208}Pb	80.0	0.832	10.2	0.874	0.62	313.8	6.24	83.6	7.97
	^{120}Sn	75.5	0.815	9.5	0.884	0.76	310.1	5.43	94.6	6.97
	^{89}Y	74.5	0.796	8.4	0.896	0.98	314.1	5.04	96.0	6.52
	^{27}Al	66.5	0.745	7.1	0.834	1.01	328.9	3.90	119.2	5.03
58.7	^{208}Pb	85.9	0.832	12.5	0.894	0.75	336.9	6.24	88.0	8.25
	^{120}Sn	82.5	0.827	12.2	0.852	0.69	338.8	5.46	88.9	7.08
	^{89}Y	80.5	0.796	10.8	0.850	1.6	339.4	5.04	98.1	6.59
	^{27}Al	71.7	0.716	9.2	0.834	0.68	354.6	3.82	130.7	5.15

$r_c = 1.30$ fm; $r_v = 1.18$ fm; $r_w = 1.27$ fm; $r_{LS} = a_{LS} = 1.00$ fm;
W_{vol} (85 MeV) = 5.0 MeV; W_{vol} (58.7 MeV) = 2.0 MeV; $V_{LS} = 6$ MeV.

extending up to angles beyond the rainbow scattering angle and the first excited states being well separated from the ground state were included. Although both conditions are not fulfilled in the cases of ^{27}Al, ^{58}Ni, and ^{103}Rh of Ref. 5, they were included for completeness. Data previously reported by our laboratory[33–36] were not considered because of problems in the absolute cross sections stemming from tailing in the Ge(Li) detectors (see the discussion of the experimental procedure in Sec. II).

Global potentials containing data with energies above 52 MeV are reported only by Daehnick *et al.*[13] In view of the expanded data base we think it is useful to derive a more recent set of global potential parameters.

The dependences of the real potential depth V, the surface absorption depth W_{surf}, and the diffuseness parameters a_v and a_w on the masses are shown in Figs. 5(a)–5(d). In Fig. 5(e) the variation with energy of the volume absorption term W_{vol} is shown. Also shown are least-square fits to the observed dependences which yield

$$V=81.33+1.43Z/A^{1/3}-0.24E_d \text{ MeV} , \tag{4a}$$

$$a_v=0.636+0.035A^{1/3} \text{ fm} , \tag{4b}$$

$$W_{\text{vol}}=\begin{cases}0.132(E_d-45) \text{ MeV for } E_d\geq 45 \text{ MeV} ,\\ 0 \text{ elsewhere} ,\end{cases} \tag{4c}$$

$$W_{\text{surf}}=7.35+1.15A^{1/3}-0.712W_{\text{vol}} \text{ MeV} , \tag{4d}$$

$$a_w=0.768+0.021A^{1/3} \text{ fm} . \tag{4e}$$

For the real potential a $Z/A^{1/3}$ term was chosen as suggested by Perey[37] to account for Coulomb corrections. In Eq. (4d) we have expressed the surface term as a function of the volume term. The quantity $W=W_{\text{surf}}+0.712W_{\text{vol}}$ appears to depend on the target mass and not the energy, whereas in Ref. 13 a dependence on the energy but not on the target mass was found.

The data were well reproduced by the potential parameters from Eqs. (4) with the exceptions of ^{12}C, ^{16}O, and ^{24}Mg at $E_d=52$ MeV where the structures in the data are still reproduced but larger χ^2/N values are observed due to (a) in the case of ^{16}O the poor reproduction of the deep and narrow minimum at $\theta=20.2°$, (b) in the case of ^{12}C the theoretical curve for angles smaller than 37° is below the data, and (c) in the case of ^{24}Mg the predictions are above the experimental data for angles larger than 20°.

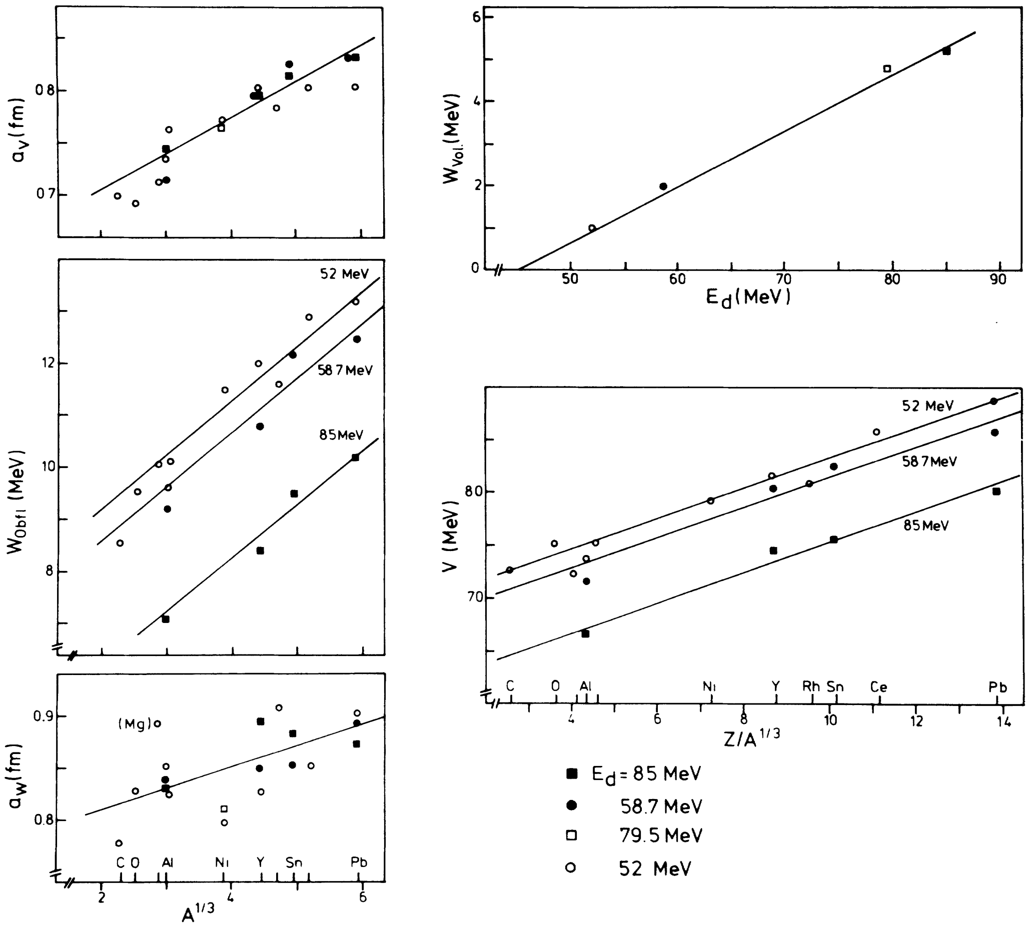

FIG. 5. The best-fit parameters together with the fits as given in Eqs. (4).

Possible explanations for these deviations have not been examined explicitly but might be due to higher-order processes.

For a better determination of the spin-orbit term data of the vector analyzing power iT_{11} measured at $E_d = 52$ MeV on a variety of nuclei[11] and of both vector analyzing power A_y and tensor analyzing power A_{yy} of 79 MeV deuteron scattering on ^{58}Ni (from Refs. 16 and 21) were included. In the following these quantities are treated in spherical coordinates as iT_{11} and As (0°). The transformation was made according to Ref. 38:

$$iT_{11} = \sqrt{3}/2 \ \ A_y$$

and

$$\mathrm{As}\ (0°) = -\tfrac{1}{2}(T_{20} + \sqrt{6}T_{22}) = A_{yy}/\sqrt{2} \ .$$

Taking only vector analyzing power data, good fits were obtained. However, the deduced parameters scatter unsystematically, and it appears to be impossible to reproduce with such an "optical potential set" the elastic cross-section data. It even was not possible to simultaneously fit both types of observables with the present spin-orbit geometry taken from a folding-model analysis. An optimum is achieved when both r_{LS} and a_{LS} are equal but mass dependent as

$$a_{LS} = r_{LS} = 0.78 + 0.038 A^{1/3} \text{ fm} \ . \tag{5}$$

Again the potential depth V_{LS} scatters around $V_{LS} = 6$ MeV. The mass dependence of the radius parameter is in agreement with folding-model predictions. In proton scattering[28,39] a mass dependence of r_{LS} but no mass dependence of the diffuseness a_{LS} was observed. Also the global deuteron potentials reported in Ref. 13 have a constant value for a_{LS}. It might be that the a_{LS} mass dependence is a consequence of the mass dependence of a_v, which was introduced to reproduce the high-energy data. The elastic cross sections were still well reproduced with this spin-orbit term. Again V_{LS} does not depend on the energy in the present investigation in contrast to potential L in Ref. 13 and the result in proton scattering.[28]

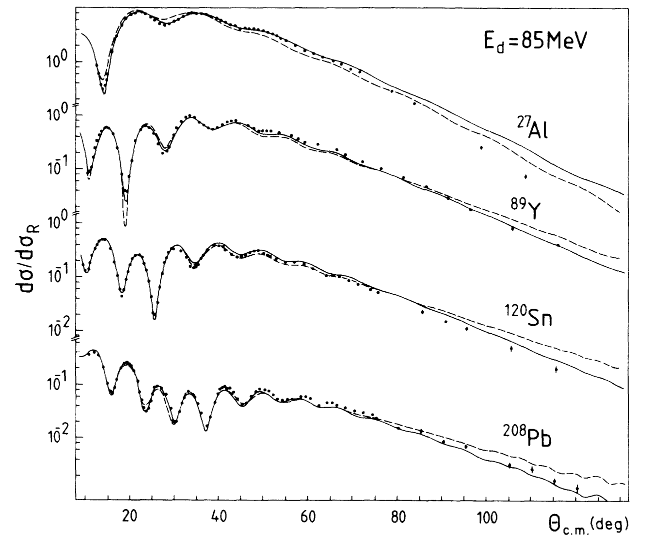

FIG. 7. Same as Fig. 6, but for $E_d = 85$ MeV.

The studies resulted in the following global potential parameters:

$$V = 81.32 + 1.43Z/A^{1/3} - 0.24E_d \text{ MeV} \ , \tag{6a}$$

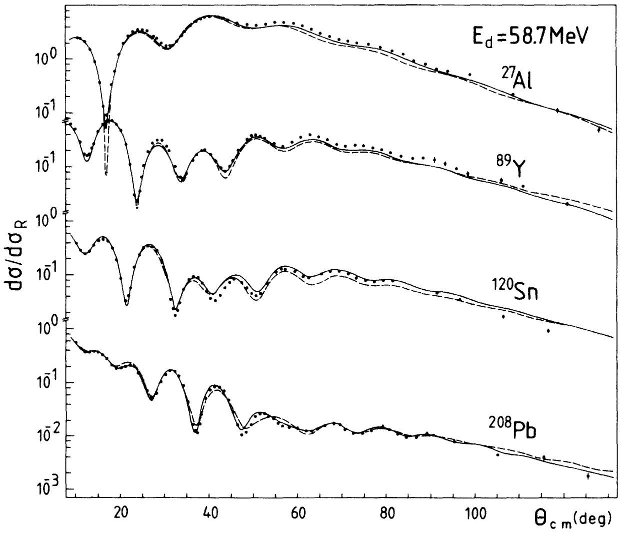

FIG. 6. Elastic angular distributions in terms of Rutherford scattering cross sections at $E_d = 58.7$ MeV. The predictions of the present global potential Eqs. (6) are shown as solid curves, those of the potential L (Ref. 13) as dashed curves.

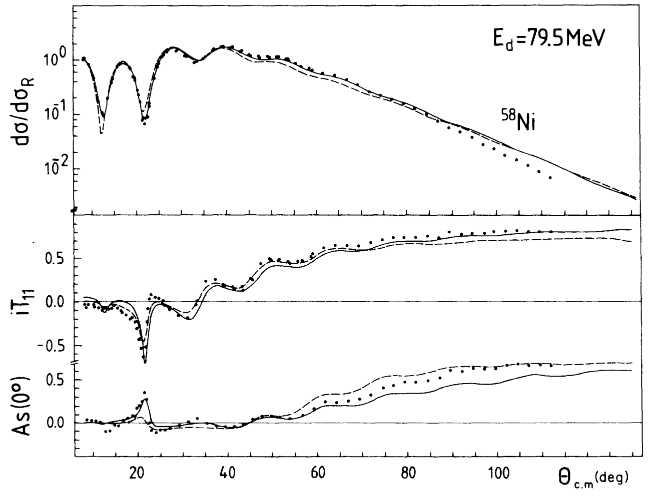

FIG. 8. Same as Fig. 6, but for $E_d = 79.5$ MeV. Also shown are the vector analyzing power iT_{11} and the asymmetry As (0°). The data are from Ref. 21.

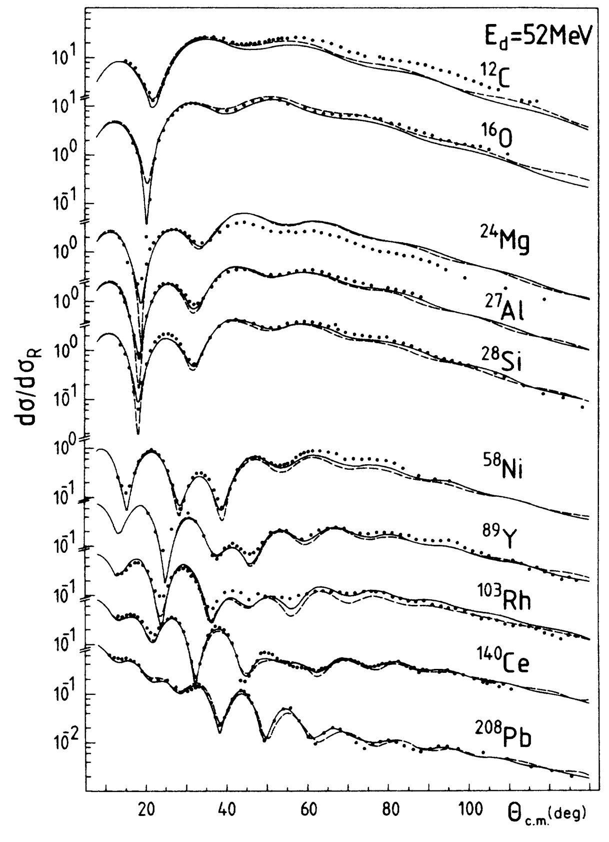

FIG. 9. Same as Fig. 6, but for $E_d = 52$ MeV. The data are from Ref. 5.

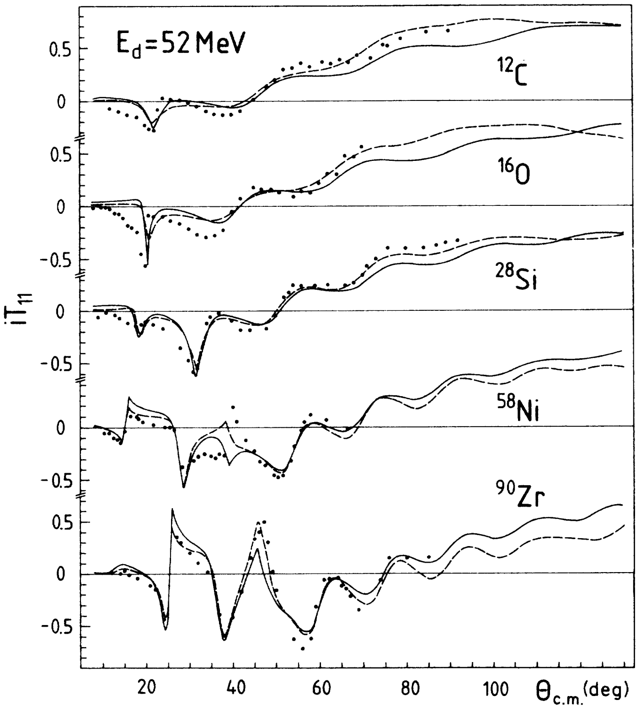

FIG. 10. Vector analyzing powers (Ref. 11) are compared with the predictions of the present global potential Eqs. (6) (solid curves) and of the potential L (Ref. 13, dashed curves).

$$r_V = 1.18 \text{ fm} , \tag{6b}$$

$$a_V = 0.636 + 0.035 A^{1/3} \text{ fm} , \tag{6c}$$

$$W_{\text{vol}} = \begin{cases} 0.132(E_d - 45) \text{ MeV for } E_d \geq 45 \text{ MeV} , \\ 0 \text{ for } E_d \leq 45 \text{ MeV} , \end{cases} \tag{6d}$$

$$W_{\text{surf}} = \begin{cases} 7.80 + 1.04 A^{1/3} - 0.712 W_{\text{vol}} \text{ MeV} , \\ \text{or 0 whichever is greater} , \end{cases} \tag{6e}$$

$$r_W = 1.27 \text{ fm} , \tag{6f}$$

$$a_W = 0.768 + 0.021 A^{1/3} \text{ fm} , \tag{6g}$$

$$V_{LS} = 6 \text{ MeV} , \tag{6h}$$

$$r_{LS} = a_{LS} = 0.78 + 0.038 A^{1/3} \text{ fm} . \tag{6i}$$

In comparison with Eqs. (4) only surface absorption and $r_{LS} = a_{LS}$ are changed. Theoretical curves calculated with this potential are compared with data in Figs. 6–10.

IV. DISCUSSION

Starting from best-fit parameters for elastic scattering cross-section data (present data and data from Refs. 5, 11, 16, and 21) a set of global optical-potential parameters [Eq. (4)] was derived with the guidance of folding-model predictions. Including the analyzing power data[11,16,21] in the analysis, the global parameters of Eq. (6) were obtained. In Figs. 6–10 the data and the predictions of both the present global potential and the nonrelativistic potential L from Ref. 13 are shown. The overall agreement appears to be reasonable. A more detailed inspection shows that especially the backward angles at the high energy for the heavy nuclei are better reproduced by the present potential. This may be because the present potential is based on data which extends to angles larger than the nuclear rainbow scattering angle, whereas potential L is based on data below 90° only. Furthermore, the analysis of Ref. 13 was based on the only data available at that time and with the emphasize on light target nuclei. The good description of the vector analyzing powers and the asymmetry is an indication that in first order the spin-orbit vector term alone is sufficient, as observed in Ref. 8 (at 30 MeV) and in Ref. 12 (at 56 MeV). Calculations with the mean geometrical parameters proposed in Ref. 11 do not reproduce our present data at 85 MeV, even with modification of all potential depths, since they predict oscillations at larger angles which are not observed in the data.

The volume integrals of the real and the imaginary potentials obtained from the best-fit searches including volume and surface absorption are listed in Table III. They do follow the systematics of Matoba *et al.*[40] The differences between the volume integrals of the present potential and potential L (Ref. 13) are small for the imaginary part and large for the real part. It has been pointed out by Greenless *et al.*[41] that the volume integral $J_V / A_p A_T$ should be determined more precisely than the potential itself; in addition, it should be less influenced by continuous ambiguities than the potential itself.

The root-mean-square (RMS) radius of the real poten-

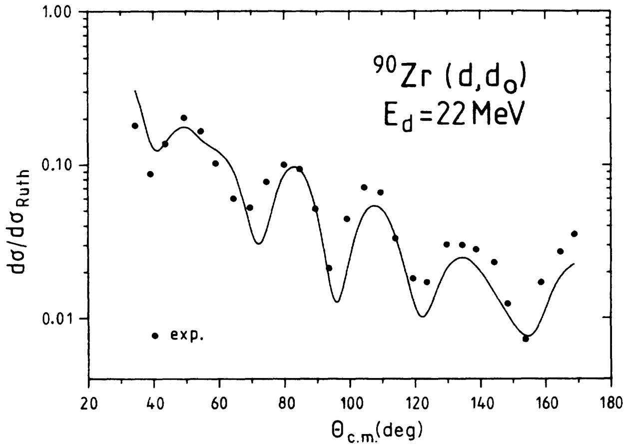

FIG. 11. Elastic angular distribution in terms of Rutherford scattering cross section at the indicated energy. The prediction of the present global potential Eqs. (6) is shown as a solid curve. The data are from Ref. 44.

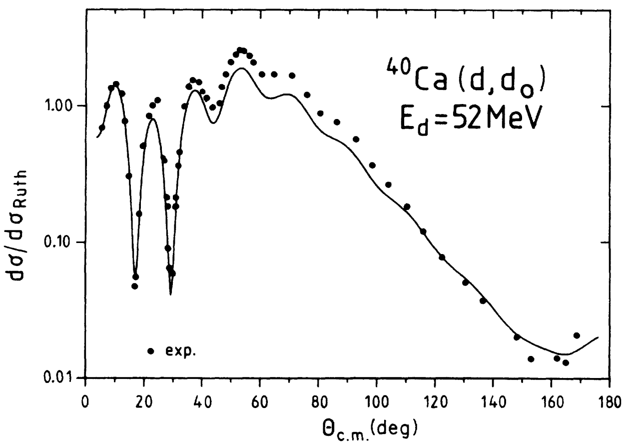

FIG. 13. Same as Fig. 11, but for the indicated reaction. Data are from Ref. 45.

tial appears to be independent of the bombarding energy potential L shows a weak energy dependence due to the energy dependence of the diffuseness parameter a_v. The present global potential shows a mass dependence of $<R_v^2>^{1/2}=1.4+0.81A^{1/3}$ fm which can be compared to the one obtained in proton scattering up to 180 MeV[28,39] of $<R_v^2>^{1/2}=1.6+0.78A^{1/3}$ fm. Comparing the RMS radii of the present global analysis to the L analysis of Ref. 13, again for the imaginary part, the results are quite similar.

The spin-orbit term is the one with the largest uncertainty in the parameters, as is discussed above and by Daehnick *et al.* The presently observed mass dependence is qualitatively in agreement with proton scattering,[28] where an even stronger mass dependence ($r_{LS} \sim A$) was observed.

Studying the question to what extent there is a need for an imaginary spin-orbit term, we have adopted a fixed geometry[9] given by the parameters $r_{WLS}=0.80$ fm and $a_{WLS}=0.20$ fm. In general, this additional term yielded a 10–20 % decrease in the χ^2/N values and in a few cases, like ^{58}Ni at 79.5 MeV, a 50% decrease. If only cross sections were analyzed, the corresponding potential depth W_{LS} scattered unsystematically around 0 MeV ±1 MeV. By fitting cross sections and vector analyzing powers simultaneously we obtained $W_{LS} \sim -0.5$ MeV with only a small scattering of the values independent of the bombarding energy. This is a much smaller value than the one ($W_{LS}=2.5$ MeV) derived in the analysis of low-energy data.[9] Also in other previous work, the imaginary spin-orbit term was found to be rather weak compared to the real one.[42] There was no significant improvement in the reproduction of the data as observed for other light ion scattering (e.g., Ref. 31). The significance of an imaginary spin-orbit term and a more precise determination of the real spin-orbit potential can only be tested with more

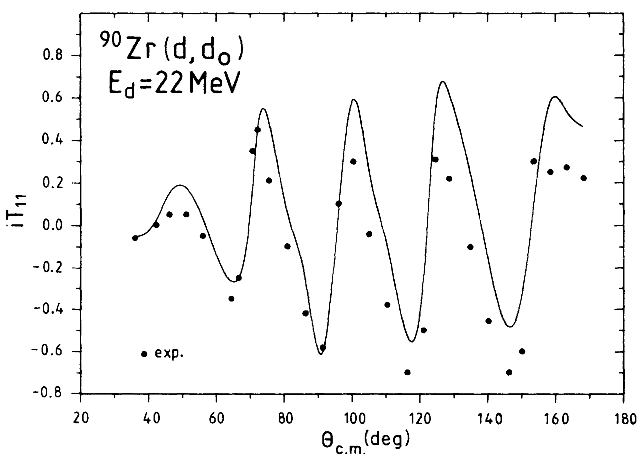

FIG. 12. Same as Fig. 11, but for analyzing power data.

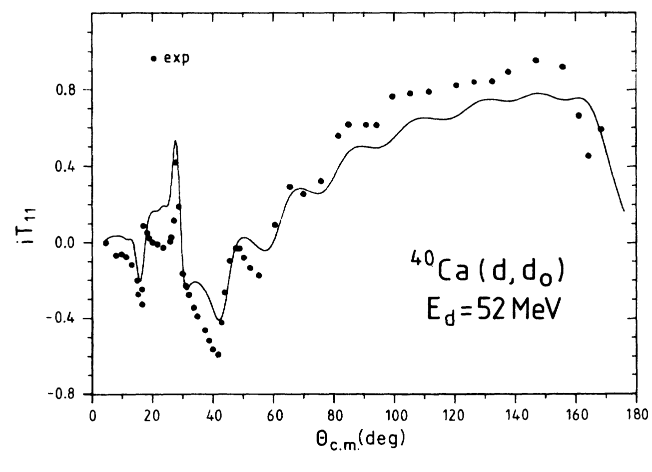

FIG. 14. Same as Fig. 13, but for analyzing power data.

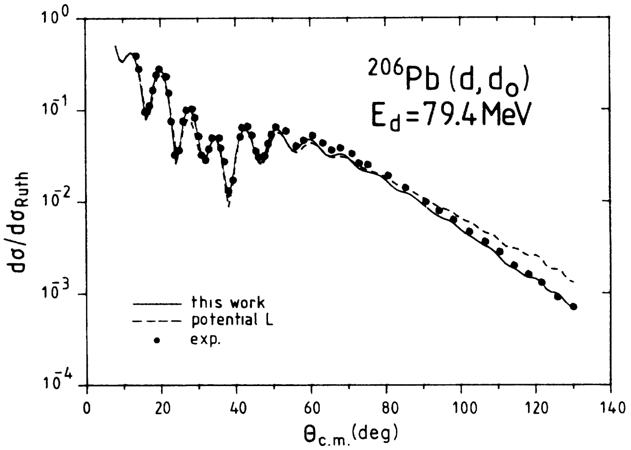

FIG. 15. Same as Fig. 11, but for the indicated reaction. The data are from Ref. 46.

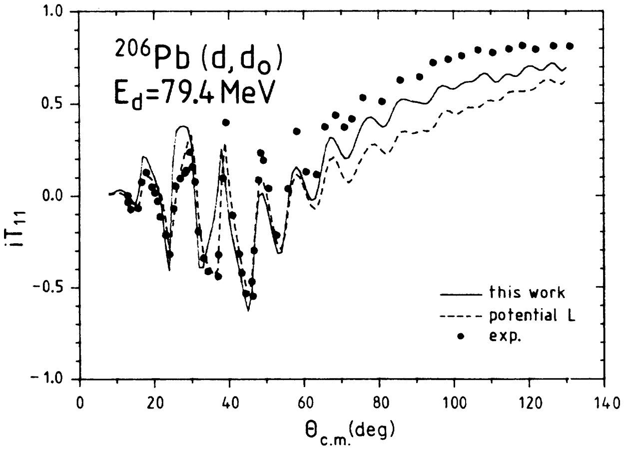

FIG. 16. Same as Fig. 15, but for analyzing power data.

high-energy data including especially analyzing powers.

A first set of such data was recently published[43] for the energy range from 200 to 700 MeV. The cross sections, vector analyzing power A_y, and tensor analyzing power A_{yy} data, were successfully described[43] within the phenomenological optical model of Eq. (1) with only volume absorption being effective. These results cannot be compared directly with ours because the geometry was allowed to vary in the search runs and the problem was treated with relativistic kinematics. We, therefore, compare only integral quantities. Up to 400 MeV the RMS radii of both the real and imaginary potential of Ref. 43 do follow the present predictions. For higher energies our potential set fails in describing the data. Similar to the potential *F* of Ref. 13 using relativistic kinematics, the volume integral of the real potential is decreasing and finally becomes negative due to a change in the sign of the potential depth *V*, whereas the analysis on Ref. 43 suggests nearly a constant volume integral for energies above 400 MeV. The volume integral of the imaginary potential agrees up to 200 MeV with the results from Ref. 43. For higher energies there is a steeper increase in the volume integral than seen in the best-fit results of Ref. 43. However, the present potential is based on data from 52 to 85 MeV, and one cannot expect the model to be applicable to energies much above this energy range. But it should be stressed that the high-energy data of Ref. 43, including the analyzing power data, are well reproduced by a potential of the form of Eq. (1) with no imaginary spin-orbit potential.

To test the predictive power of the present global optical-potential parameter set [Eqs. (6)] we have compared calculated quantities with data which were not included in the data analysis. The first example, shown in Figs. 11 and 12, deals with a rather small bombarding energy ($E_d = 22$ MeV) which is an extrapolation of the present global potential to low energies. The elastic cross section as well as the analyzing power[44] are produced. The same is true for data at $E_d = 52$ MeV (Ref. 45) and $E_d = 79.4$ MeV (Ref. 46). In the case of the deuteron scattering at $E_d = 52$ MeV on ^{40}Ca, the cross section is reproduced quite well, while the analyzing power data cannot be reproduced around 20° (Figs. 13 and 14). In the case of ^{206}Pb at 79.4 MeV it was possible to achieve with the present potential a reasonable reproduction of the data (Figs. 15 and 16) without employing an imaginary spin-orbit term, as was introduced by Radhakrishna *et al.*[46]

ACKNOWLEDGMENTS

The authors acknowledge Professor C. Mayer-Böricke for his interest and support in the initial stage of this work. We further gratefully acknowledge the efforts of the detector and target laboratory in providing the excellent support necessary for the present experiments.

---

[1] H. Feshbach, C. E. Porter, and V. E. Weisskopf, Phys. Rev. **96**, 448 (1965).

[2] T. Becker, Phys. Lett. **5**, 331 (1963).

[3] C. M. Perey and F. G. Perey, Phys. Rev. **132**, 775 (1963); **134**, B353 (1964).

[4] C. M. Perey and F. G. Perey, Phys. Rev. **152**, 923 (1966).

[5] F. Hinterberger, G. Mairle, U. Schmidt-Rohr, G. J. Wagner, and P. Turek, Nucl. Phys. **A111**, 265 (1968).

[6] J. D. Childs, W. W. Daehnick, and M. J. Spisac, Phys. Rev. C **10**, 217 (1974).

[7] P. Schwandt and W. Haeberli, Nucl. Phys. **A123**, 401 (1969).

[8] G. Perrin *et al.*, Nucl. Phys. **A282**, 221 (1977).

[9] R. P. Goddard and W. Haeberli, Nucl. Phys. **A316**, 116 (1979).

[10] H. R. Bürgi *et al.*, Nucl. Phys. **A334**, 413 (1980).

[11] G. Mairle *et al.*, Nucl. Phys. **A339**, 61 (1980).

[12] K. Hatanaka *et al.*, Nucl. Phys. **A340**, 93 (1980).

[13] W. W. Daehnick, J. D. Childs, and Z. Vrcelj, Phys. Rev. C **21**, 2253 (1980).

[14] C. M. Perey and F. G. Perey, At. Data Nucl. Data Tables **17**, 1 (1976).

[15] R. P. Goddard and W. Haeberli, Phys. Rev. Lett. **40**, 701 (1978).

[16] E. J. Stephenson, C. C. Foster, P. Schwandt, and D. A. Goldberg, Nucl. Phys. **A359**, 316 (1981).

[17] F. G. Perey and G. R. Satchler, Nucl. Phys. **A97**, 515 (1967).

[18] P. W. Keaton and D. D. Armstrong, Phys. Rev. C **8**, 1682 (1973).

[19] G. H. Rawitscher and S. N. Mukherjee, Nucl. Phys. **A342**, 90 (1980).

[20] A. A. Ioannides and R. C. Johnson, Phys. Rev. C **17**, 1331 (1978).

[21] E. J. Stephenson *et al.*, Phys. Rev. C **28**, 134 (1983).

[22] N. Austern *et al.*, Phys. Rep. **154**, 125 (1987).

[23] K. W. Ford and J. A. Wheeler, Ann. Phys. (N.Y.) **7**, 259 (1959); **7**, 287 (1959).

[24] D. A. Goldberg *et al.*, Phys. Rev. C **7**, 1938 (1973); **10**, 1362 (1974).

[25] G. Riepe and D. Protić, Nucl. Instrum. Methods **101**, 77 (1972).

[26] J. Bojowald, H. Machner, W. Oelert, M. Rogge, and P. Turek, Nucl. Instrum. Methods **A253**, 298 (1987).

[27] J. Bojowald, Ph.D. Thesis, Institut für Kernphysik 1984.

[28] A. Nadasen *et al.*, Phys. Rev. C **23**, 1023 (1981).

[29] G. R. Satchler, Nucl. Phys. **21**, 116 (1960).

[30] J. Raynal, optical model code MAGALI, Centre d' Etúdes Nucleaires Saclay Report No. DPH-T/69-42, 1969 (unpublished).

[31] R. A. Hardekopf *et al.*, Phys. Rev. Lett. **35**, 1623 (1975).

[32] A. Bohr and B. Mottelson, *Nuclear Structure* (Benjamin, New York, 1969), Vol. I.

[33] G. Hrehuss *et al.*, Z. Phys. **260**, 179 (1973).

[34] O. Aspelund *et al.*, Nucl. Phys. **A253**, 263 (1975).

[35] A. Kiss *et al.*, Nucl. Phys. **A262**, 1 (1976).

[36] K. T. Knöpfle *et al.*, Phys. Rev. C **13**, 1400 (1976).

[37] F. G. Perey, Phys. Rev. **131**, 745 (1963).

[38] *Proceedings of the 3rd International Symposium on Polarization Phenomena*, edited by H. H. Barshall and W. Heaberli (University of Wisconsin Press, Madison, 1971), p. xxv.

[39] W. T. H. van Oers *et al.*, Phys. Rev. C **10**, 307 (1974).

[40] M. Matoba, M. Hyakutake, and I. Kumabe, Phys. Rev. C **32**, 1773 (1985).

[41] G. W. Greenlees, G. J. Pyle, and Y. C. Tang, Phys. Rev. **171**, 1115 (1968).

[42] G. Szaloky, L. A. Montestruque, M. C. Cobian-Rozak, and S. E. Darden, Phys. Rev. C **18**, 750 (1978).

[43] Nguyen Van Sen *et al.*, Phys. Lett. **156B**, 185 (1985).

[44] M. Takei *et al.*, J. Phys. Soc. Jpn. Suppl. **55**, 676 (1986).

[45] M. Ermer *et al.*, Phys. Lett. B **188**, 17 (1987).

[46] M. C. Radhakrishna *et al.*, Phys. Rev. C **37**, 66 (1988).